Cubic-type Heusler compound Mn₂FeGa thin film with strain-induced large perpendicular magnetic anisotropy

Phillip David Bentley [1], Songtian Li [1,*], Keisuke Masuda [2], Yoshio Miura,[2,3] Ye Du,[1] Takaya Mitsui,[1,4]
Kosuke Fujiwara [4], Yasuhiro Kobayashi [5], Tengyu Guo,[6] Guoqiang Yu,[6,7] Chihiro Suzuki,[1] Shunya Yamamoto [1],
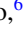Fu Zheng,[8] Yuya Sakuraba,[2] and Seiji Sakai [1,†]

[1]*Quantum Materials and Applications Research Center, National Institutes for Quantum Science and Technology, Takasaki 370-1292, Japan*
[2]*Research Center for Magnetic and Spintronic Materials, National Institute for Materials Science, Sengen 1-2-1, Tsukuba 305-0047, Japan*
[3]*Center for Spintronics Research Network, Osaka University, Toyonaka 560-8531, Japan*
[4]*Synchrotron Radiation Research Center, National Institutes for Quantum Science and Technology, Sayo, Hyogo 679-5148, Japan*
[5]*Institute for Integrated Radiation and Nuclear Science, Kyoto University, Asashironishi, Kumatori, Osaka 590-0494, Japan*
[6]*Songshan Lake Materials Laboratory, Dongguan, Guangdong 523808, China*
[7]*Beijing National Laboratory for Condensed Matter Physics, Institute of Physics, Chinese Academy of Sciences, Beijing 100190, China*
[8]*School of Physics and Electronic-Electrical Engineering, Ningxia University, Yinchuan 750021, China*

This study reports the development of ferrimagnetic cubic Heusler compound Mn_2Fe_xGa (MFG) thin films with large perpendicular magnetic anisotropy (PMA). By growing MFG on a Cr buffer layer, a cubic X_a phase with a tetragonal distortion $c/a \approx 1.04$ induced by the buffer layer was obtained in the range of $x = 1.0$–1.3, leading to large PMA which exceeds 0.75 MJ m^{-3} in stoichiometric Mn_2FeGa ($x = 1$). Synchrotron Mössbauer spectroscopy revealed that these cubic MFG thin films show good chemical ordering close to the X_a-ordered state. First-principles calculations demonstrated that, in X_a-ordered cubic MFG, the characteristic electronic structure of Fe around the Fermi level causes a large uniaxial magnetocrystalline anisotropy under the tetragonal strain consistent with experiment. The half-metallic-like band structure of cubic MFG was also shown to be preserved under the strain. Cubic Mn_2FeGa with its small saturation magnetization, large PMA, and possibility of being highly spin polarized make this material an ideal candidate for the development of magnetic random-access memory and other spintronic devices.

I. INTRODUCTION

Possessing a half-metallic band structure at the Fermi level, Heusler compounds are considered one way of achieving highly spin-polarized current and large magnetoresistance in various spintronic devices [1,2]. Over the past few decades, there has been significant focus towards Co_2YZ-type full-Heusler compounds [cubic $L2_1$ crystal structure ($Fm\bar{3}m$)] due to numerous observations of high spin polarization and ultralow damping in Co_2YZ-based spin valves [3–13]. More recently, topological Weyl states have been observed in Co_2MnGa Heusler compounds broadening the interest of using Co_2YZ-type Heusler compounds in applications such as magnetization switching by spin-orbit torque [14,15]. While these Heusler compounds possess electronic band structures suitable for spintronic applications, their magnetization has also been found to be in plane, which has so far limited their application in ultrahigh density spintronic devices [16].

Recently, Mn_2YZ-type Heusler compounds with cubic X_a crystal structure ($F\bar{4}3m$) have been of increasing interest in spintronics. In contrast to Co_2YZ-type Heusler compounds,

perpendicular magnetic anisotropy (PMA) has been demonstrated in cubic Mn_2Ru_xGa (MRG) and Mn_2Co_xGa (MCG) thin films [17,18]. In addition to PMA and predicted half-metallicity, cubic-type Mn_2YZ-type Heusler compounds also show a small saturation magnetization (M_s) due to their ferrimagnetic ordering along with the possibility of a fully compensated magnetic moment at specific compositions and temperatures [17,19]. Achieving high spin polarization, PMA, and small M_s could make Mn_2YZ-type Heusler compounds promising materials for spintronic applications and the realization of low energy consumption, high density, and ultrafast switching magnetic random-access memory.

In this paper, we report the realization of large PMA in thin films of cubic-type full-Heusler compound Mn_2Fe_xGa (MFG) with an atomic ordering close to the X_a inverse full-Heusler crystal structure. Previous theoretical studies have predicted that X_a-ordered cubic Mn_2FeGa is a metastable phase with a half-metallic-like band structure [20–22], yet the majority of studies so far have only managed to synthesize tetragonal (DO_{22}) MFG. While tetragonal MFG and other tetragonal compounds such as Mn_3Ga and Mn_3Ge exhibit large PMA [23–28], the spin polarization at the Fermi level of tetragonal MFG is also significantly reduced due to the filling of the energy gap in the minority band [22]. Most strikingly, these cubic MFG thin films show large PMA exceeding $K_u = 0.75$ MJ m^{-3}, which is far above the values reported

*li.songtian@qst.go.jp
†sakai.seiji@qst.go.jp

for other cubic ferrimagnetic Heusler compounds [18,29]. Furthermore, synchrotron Mössbauer spectroscopy along with theoretical calculations provides direct evidence of these cubic MFG thin films having a high degree of chemical ordering and being highly spin polarized, thus making MFG an ideal candidate material for use in various spintronic devices.

II. EXPERIMENTAL METHODS

Thin films of Mn_2Fe_xGa with Fe concentrations $x \approx 0.8$, 1.0, and 1.3 were prepared on MgO(001) single crystal substrates using Cr thin films as a buffer layer. MgO substrates were furnace treated prior in air at 1173 K. 20 nm thick Cr buffer layers were deposited at room temperature and then annealed at 940 K. The MFG thin films were grown by co-sputtering a Mn_2Ga target and a Fe target while maintaining the substrate at 570 K. To control the stoichiometry of the MFG thin films, the sputtering power applied to the Fe target was changed to vary the Fe concentration. The stoichiometry of the MFG thin films was later evaluated by energy-dispersive x-ray spectroscopy (EDS). The samples of MFG thin films on Cr buffer layers (MFG/Cr, hereafter) were capped with a 1 nm thick Al layer to prevent oxidation of the MFG.

Transmission electron microscope (TEM) images were obtained using a JEOL JEM-2100F TEM operated at an accelerating voltage of 200 kV. X-ray diffraction (XRD) analysis was performed using an x-ray diffractometer with a Cu $K\alpha_1$ x-ray source. The magnetic properties of the MFG thin films were investigated using a Quantum Design MPMS3 superconducting quantum interference device (SQUID). All the magnetization data presented here were corrected for the linear diamagnetic background of the MgO substrate. To gain insight into the local atomic structure and chemical ordering of MFG in the MFG/Cr samples, synchrotron ^{57}Fe Mössbauer spectroscopy was performed at the BL11XU beamline of SPring-8 using linearly π-polarized 14.4 keV Mössbauer γ rays [30]. A grazing incidence conversion electron Mössbauer spectroscopy (CEMS) technique with a probing depth of several 10 nm was used to detect the whole region of the MFG thin film. The γ-ray beams were incident on the film surface at a low glazing angle of $0.5°$ to increase the effective thickness of the thin films. The use of the high-brilliance synchrotron Mössbauer γ rays in combination with the grazing incidence CEMS technique allowed the measurement efficiency to be improved dramatically [31,32].

III. COMPUTATIONAL METHODS

The electronic structure of cubic Mn_2FeGa was calculated using the Vienna *ab initio* simulation program (VASP) and density-functional theory (DFT) which included the spin-orbit interaction (SOI) in the calculation [33]. X_a-ordered Mn_2FeGa with lattice constants of $a=5.83$ Å and $c=6.07$ Å (with tetragonal distortion) as well as $a = c = 5.83$ Å (without tetragonal distortion) were considered based on the values determined by XRD. In the DFT calculation, the generalized gradient approximation (GGA) [34] was adopted for the exchange-correlation energy and a projected augmented wave pseudopotential was used [35,36] to treat the effect of core

electrons properly. The cutoff energy was set to 337 eV and the Brillouin-zone integration was performed with $31 \times 31 \times 31$ k points.

The uniaxial magnetocrystalline anisotropy K_u of cubic Mn_2FeGa was calculated on the basis of these DFT results, where the following expression derived from the force theorem [37,38] was used for the calculation:

$$K_u = (E_{[100]} - E_{[001]})/V, \qquad (1)$$

where $E_{[100]}$ ($E_{[001]}$) is the sum of the eigenenergies for the unit cell with the magnetization parallel to the [100] ([001]) direction, and V is the volume of the unit cell.

To investigate the physical origin of the perpendicular magnetic anisotropy (PMA), a second-order perturbation analysis of the magnetocrystalline energy was further carried out [39]. By treating the SOI as a perturbation term, the second-order perturbation energy is given by the following equations:

$$E^{(2)} = \sum_{\boldsymbol{k}} \sum_{n'\sigma'}^{\text{unocc}} \sum_{n\sigma}^{\text{occ}} \frac{|\langle \boldsymbol{k}n'\sigma'|H_{\text{SOI}}|\boldsymbol{k}n\sigma\rangle|^2}{\epsilon_{\boldsymbol{k}n\sigma}^{(0)} - \epsilon_{\boldsymbol{k}n'\sigma'}^{(0)}}, \qquad (2)$$

$$H_{\text{SOI}} = \sum_i \xi_i \boldsymbol{L}_i \cdot \boldsymbol{S}_i, \qquad (3)$$

where $\epsilon_{\boldsymbol{k}n\sigma}^{(0)}$ is the energy of an unperturbed state $|\boldsymbol{k}n\sigma\rangle$ with wave vector $\boldsymbol{k}$, band index n, and spin σ. The index "occ" ("unocc") on the summation in Eq. (2) means that the sum is over the occupied (unoccupied) states of all atoms in the unit cell. In the H_{SOI}, ξ_i is the coupling constant of the SOI at an atomic site i, and $\boldsymbol{L}_i$ ($\boldsymbol{S}_i$) is the single-electron angular (spin) momentum operator. For ξ_i, $\xi_{\text{Mn}} = 41.5$ meV, $\xi_{\text{Fe}} = 54.3$ meV, and $\xi_{\text{Ga}} = 35.4$ meV were used, respectively. Wave functions and eigenenergies obtained in the DFT calculation were used as unperturbed states and energies in Eq. (2). The magnetocrystalline anisotropy energy within the second-order perturbation was calculated as $E_{\text{MCA}}^{(2)} = E_{[100]}^{(2)} - E_{[001]}^{(2)}$ similarly to Eq. (1), where $E_{[100]}^{(2)}$ ($E_{[001]}^{(2)}$) is the energy calculated by Eq. (2) for the magnetization along the [100] ([001]) direction of the unit cell. $E_{\text{MCA}}^{(2)}$ can be decomposed into four terms coming from different perturbation processes at each atomic site:

$$E_{\text{MCA}}^{(2)} = \sum_i E_{\text{MCA}}^i, \qquad (4)$$

$$E_{\text{MCA}}^i = \Delta E_{\uparrow \Rightarrow \uparrow}^i + \Delta E_{\downarrow \Rightarrow \downarrow}^i + \Delta E_{\uparrow \Rightarrow \downarrow}^i + \Delta E_{\downarrow \Rightarrow \uparrow}^i, \quad (5)$$

where E_{MCA}^i is the magnetocrystalline anisotropy energy at an atomic site i. The term $\Delta E_{\uparrow \Rightarrow \uparrow}^i$ ($\Delta E_{\downarrow \Rightarrow \downarrow}^i$) is the contribution from spin-conserving perturbation processes in the majority spin (minority spin) channel. The last two terms are the contributions from spin-flip perturbation processes: $\Delta E_{\uparrow \Rightarrow \downarrow}^i$ ($\Delta E_{\downarrow \Rightarrow \uparrow}^i$), which come from the electron transition processes from the majority to minority spin (minority to majority spin) channel. This decomposition provides information on the origin of PMA in cubic MFG.

Furthermore, the type of possible chemical disorder in the cubic MFG thin films and its influence on the electronic structure were theoretically simulated for cubic Mn_2FeGa with a tetragonal distortion for comparison with the Mössbauer results. Here three types of states of Mn_2FeGa were considered: the X_a-ordered state, $L2_1B$-ordered state with disorder
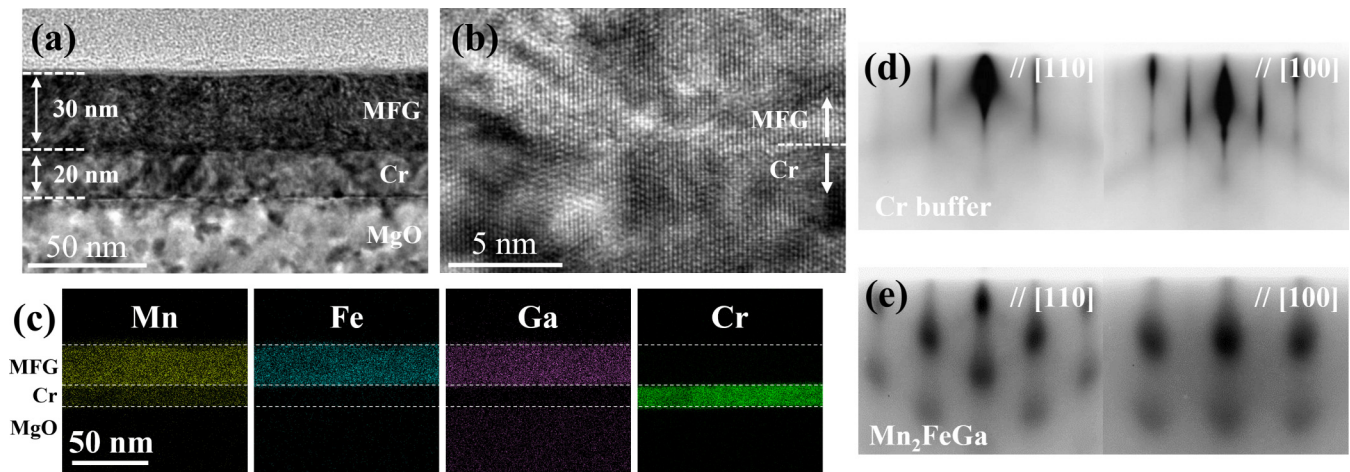
FIG. 1. (a) Bright field cross-sectional TEM image for the stoichiometric Mn$_2$FeGa (30 nm)/Cr (20 nm)/MgO(001) sample. (b) High-resolution TEM image of the MFG/Cr interface. (c) EDS mapping results for the image shown in part (a). RHEED patterns along the [110] and [100] azimuths of the MgO(001) substrate for (d) a 20 nm thick Cr buffer grown on the MgO(001) substrate and (e) a 30 nm thick stoichiometric MFG thin film grown on top of the Cr buffer layer.

between the Mn 4a and Fe 4b atomic sites, and the D0$_3$-ordered state with disorder between the Mn 4c and Fe 4b sites (the locations of these sites can be seen in the inset of Fig. 6) [40]. These calculations were based on DFT and the Korringa-Kohn-Rostoker method [41,42], which are implemented in the Akai-KKR code [43]. In these calculations, the GGA [34] was used for the exchange-correlation energy and the disordered states were treated within the coherent potential approximation. The Brillouin-zone integration was performed with 10^3 and 15^3 k points in the self-consistent-field and DOS calculations, respectively.

IV. RESULTS AND DISCUSSION

A. Structural characteristics

Figures 1(a) and 1(b) show TEM images obtained for a stochiometric Mn$_2$FeGa (30)/Cr (20)/MgO(001) sample (thicknesses in nm indicated in brackets). The bright field cross-sectional image [Fig. 1(a)] shows clear interfaces between each of the layers, and the high-resolution TEM image [Fig. 1(b)] shows the MFG/Cr interface to be atomically coherent. The EDS mapping in Fig. 1(c) shows the distributions of Mn, Fe and Ga to be homogeneous across the entire MFG thin film and no evidence of interdiffusion was observed. Reflection high-energy electron diffraction (RHEED) patterns measured along the [110] and [100] azimuths of the MgO(001) substrate for a 20 nm Cr buffer layer and (c) the stoichiometric 30 nm MFG thin film grown on top of this Cr buffer layer are shown in Figs. 1(d) and 1(e), respectively. The evolution of the RHEED patterns shows that a single crystalline MFG thin film is grown on a Cr buffer layer with an epitaxial relationship of MFG(001)[100] ∥ Cr(001)[100] ∥ MgO(001)[110]. The streak-shaped patterns from the Cr buffer layer indicate an atomically flat Cr surface with a $c(2\times2)$ surface reconstruction due to the adsorption of oxygen at the topmost surface of the Cr buffer layer [44]. This surface reconstruction is found not to influence the subsequent growth of the MFG thin film. For the MFG thin film, spotty RHEED patterns are observed

indicating an increase in surface roughness, but with this being limited based on the cross-sectional TEM image seen in Fig. 1(a) and the atomic force microscopy (AFM) image of a larger area (see the Supplemental Material [45]).

Figure 2(a) shows the XRD profiles of the MFG/Cr samples with $x = 0.8$, 1.0, and 1.3. For $x = 0.8$, both cubic X$_a$ and tetragonal DO$_{22}$ phases were observed. The formation of tetragonal MFG below $x = 1.0$ was reported in an earlier study [46]. The tetragonal phase was found to be suppressed with increasing the Fe concentration, and only a cubic phase was observed in the range of $x \geqslant 1.0$. The XRD profiles of the stoichiometric MFG/Cr sample ($x = 1.0$) measured for the (111) and (110) crystallographic planes are shown in
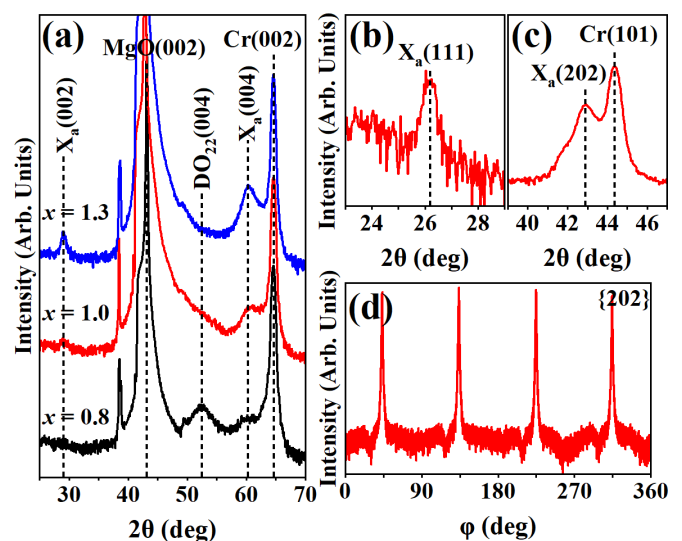

FIG. 2. (a) The XRD profiles of the MFG/Cr samples with Fe concentrations, $x = 0.8$, 1.0, and 1.3 respectively. (b) and (c) XRD profiles of the MFG/Cr sample with $x = 1.0$ for the (111) and (110) crystallographic planes, respectively. (d) ϕ scan of the (202) reflection.

Figs. 2(b) and 2(c), respectively. The presence of the (111) reflection in Fig. 2(b) indicates chemical ordering of the X_a structure. The fourfold symmetric {202} peaks as seen in Fig. 2(d) confirm high-quality epitaxial growth of MFG on a Cr buffer layer.

The in-plane (a) and out-of-plane (c) lattice constants of cubic MFG in the MFG/Cr samples were calculated from the (004) and (202) reflections due to the X_a structure. Cubic MFG was found to show lattice constants $a \approx 5.78$–5.84 Å and $c \approx 6.06$–6.11 Å, slightly depending on the sample composition (for $x = 1.0$, $a \approx 5.83$ Å and $c \approx 6.07$ Å) (similar values were also obtained from the selected area electron diffraction patterns in TEM; see the Supplemental Material [45]). This indicates that a tetragonal strain λ of 4–6 %, where $\lambda = 100 \times (c - a)/a$, was induced in the cubic MFG thin films due to the lattice matching between cubic MFG and Cr (lattice constant found to be $a \approx 2.88$ Å) under the epitaxial relationship, although the in-plane lattice constants of cubic MFG remain close to the theoretically calculated values [20,22]. A similar phenomenon has been observed in MRG and MCG thin films grown on buffer layers [17,18].

Since the intensity ratios between certain peaks reflect chemical ordering within Heusler compounds [6], the intensity ratios of the (200) and (400) reflections and the (111) and (444) reflections were calculated to be 0.25 and 0.058 for the stoichiometric MFG/Cr sample, respectively. In comparison, theoretical values for X_a-ordered Mn_2FeGa were calculated to be 0.33 and 0.036, respectively. The differences between the experimental and theoretical values suggest the presence of chemical disorder in cubic MFG. However, it is difficult to discuss the degree of chemical ordering due to the similar scattering factors of Mn and Fe, as pointed out in an earlier study [47]. Thus, in this study synchrotron Mössbauer spectroscopy was used to obtain insight on the local atomic structure and chemical ordering in cubic MFG, as presented in Sec. IV C.

B. Magnetic properties

Figure 3(a) shows the in-plane (IP) and out-of-plane (OP) magnetization curves for the stoichiometric MFG/Cr sample. It was found that all the MFG/Cr samples in the composition range $0.8 \leqslant x \leqslant 1.3$ show a clear out-of-plane easy axis of magnetization. In the case of the stoichiometric MFG/Cr sample composed of cubic MFG, the OP curve showed a square shape and large coercive field, meanwhile the IP curve showed no saturation by 7 T, which is the upper limit of the SQUID system used. The saturation magnetic moment M_s is approximately 1.2 μ_B/f.u. which is close to the expected moment 1.0 μ_B/f.u. predicted by the Slater-Pauling rule for full-Heusler compounds [48,49] and also the theoretically calculated value (see the Supplemental Material [45]). This confirms the ferrimagnetic ordering in cubic MFG. The magnetic anisotropy constant K_u was evaluated from the data in Fig. 3(a) using the following equation:

$$K_u = \frac{1}{2}H_k \cdot M_s \qquad (6)$$

where H_k is the anisotropy field. Since the IP magnetization is not saturated by 7 T, the lower bound of $K_u \approx 0.75$ MJ m^{-3} was found by setting $H_k \geqslant 7$ T. Compared to other cubic
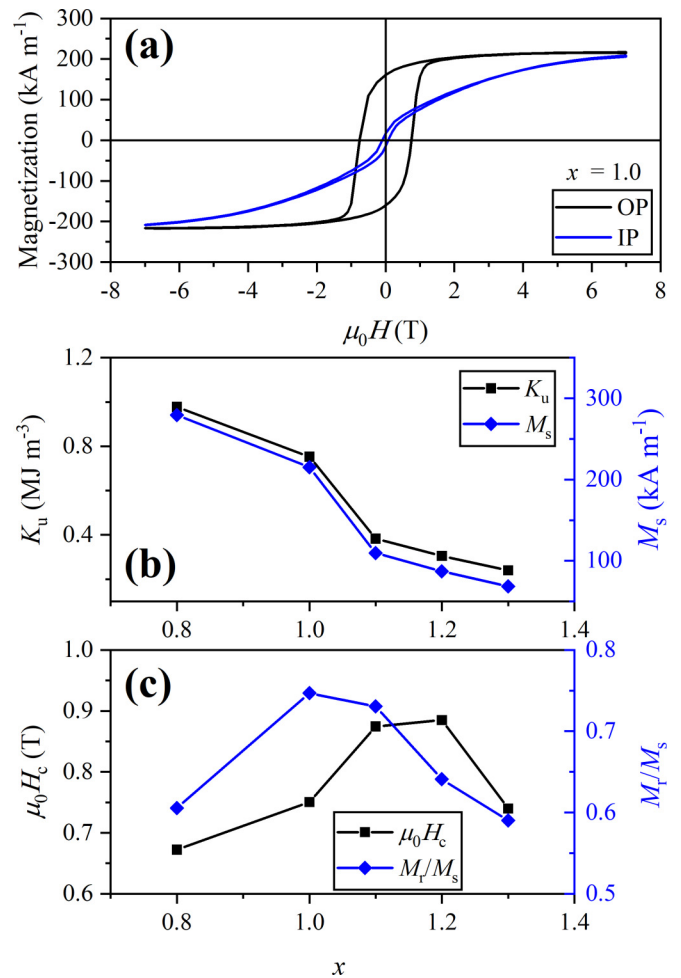

FIG. 3. (a) In-plane (IP) and out-of-plane (OP) magnetization curves measured at room temperature for the stoichiometric MFG/Cr sample. (b) Magnetic anisotropy constant (K_u) and saturation magnetization (M_s) as a function of Fe concentration x. (c) Magnetic coercivity ($\mu_0 H_c$) and squareness of the hysteresis loop (M_r/M_s) also a function of x.

Heusler compounds, K_u of cubic MFG is quite large: the largest values that have ever been observed in any cubic Heusler compound, far exceeding that of MRG (50 kJ m^{-3}) and MCG (0.16 MJ m^{-3}) [18,29].

As seen in Fig. 3(b), increasing the Fe concentration above $x = 1.0$ leads to both a decrease in M_s and the lower bound of K_u (the magnetization curves for each sample are shown in the Supplemental Material [45]). As is discussed in Sec. IV C, the reduction in M_s with increasing x can be attributed to increased chemical disorder where excess Fe forms antisite defects by occupying the Mn $4a$ sites (see the inset of Fig. 6). This is due to the ground state energy of the L2$_1$B-ordered state being 0.26 eV lower than the D0$_3$-ordered state from theoretical calculations (see the Supplemental Material [45]) implying that excess Fe preferably occupies the Mn $4a$ atomic site over the Mn $4c$ site. It is worth noting that H_k was larger than 7 T for all samples with different x. Figure 3(c) shows the magnetic coercivity ($\mu_0 H_c$) and squareness (M_r/M_s) of the different MFG/Cr samples. The coercivity was found to increase with increasing x until
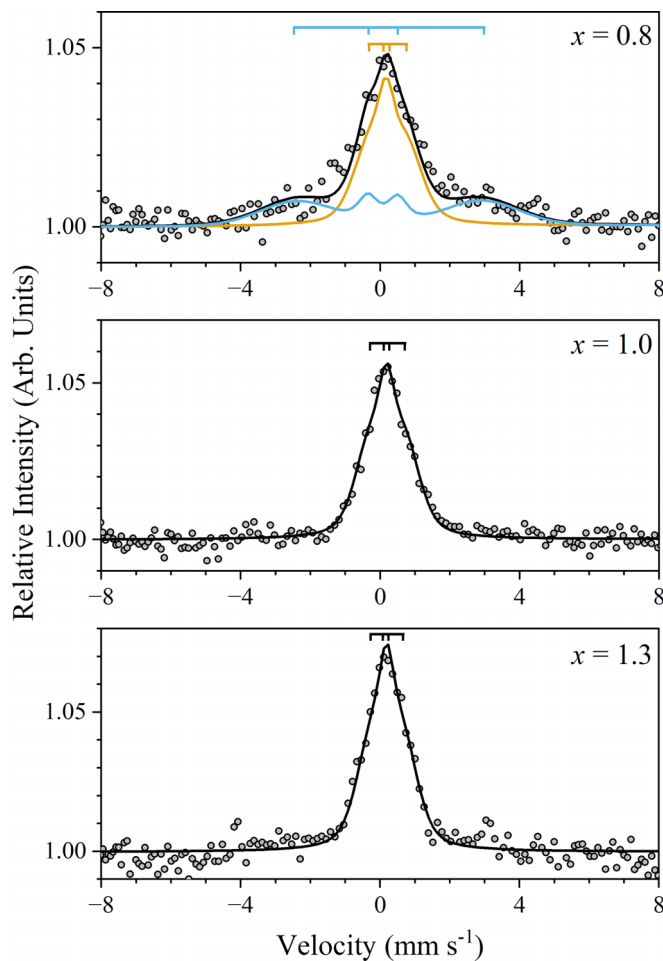
FIG. 4. Mössbauer spectra of MFG/Cr samples with different Fe concentrations (x). The sample with $x = 0.8$ shows a peak which is a convolution of two magnetic components: the blue component due to the presence of tetragonal MFG and the golden component due to cubic MFG. For the samples with $x = 1.0$ and 1.3, only a single component due to cubic MFG was observed. The fitted peak positions are highlighted by the bars above each spectrum.

$x = 1.2$, where it then decreased for $x = 1.3$. The squareness was found to be at a maximum for the stoichiometric MFG/Cr sample but then proceeded to decrease with lower or higher Fe concentrations. The largest M_r/M_s value at $x = 1$ implies high structural homogeneity of the MFG thin film with stoichiometric composition because the remanence strongly depends on microstructural features such as grain size, its distribution, and defects [23,50].

C. Local atomic structure and chemical ordering

Figure 4 shows the Mössbauer spectra of the MFG/Cr samples with $x = 0.8$, 1.0, and 1.3. Due to the perpendicular magnetization of each sample, the π-polarized incident beam only interacts with the four nuclear transitions with $\Delta m = \pm 1$. Therefore, the isomer shift δ, quadrupole shift 2ε, and hyperfine field H_{int} were derived from the four-line spectra using the Voigt function by considering the hyperfine field distribution, ΔH_{int} [51], as summarized in Table I. It was found that the MFG thin films were composed of ei-

TABLE I. Experimental hyperfine parameters for MFG/Cr samples with different Fe concentrations (x). A represents the area percentage of the magnetic component (and its color), δ is the isomer shift, H_{int} is the internal magnetic hyperfine field, 2ε is the quadruple shift, ΔH_{int} is the hyperfine field distribution, and M_{Fe} is the Fe magnetic moment.

x	A (%)	δ (mm/s)	H_{int} (T)	2ε (mm/s)	ΔH_{int} (T)	M_{Fe} (μ_B)
0.8	57 (gold)	0.20	3.4	0.0	5.0	0.27
	43 (blue)	0.17	16.5	0.2	14.2	1.32
1.0	100 (black)	0.20	3.1	0.0	4.7	0.25
1.3	100 (black)	0.19	2.8	0.0	4.6	0.22

ther a single magnetic component or a convolution of two magnetic components depending on the Fe concentration. The MFG/Cr samples with $x = 1.0$ and $x = 1.3$ composed of the cubic phase exhibited a single magnetic component with a small internal magnetic hyperfine field $H_{\text{int}} \sim 3$ T and zero quadrupole shift. Using a hyperfine coupling constant of 12.5 T/μ_B, which has been adopted for Fe₂YZ-type Heusler compounds [52], the magnetic moment M_{Fe} of Fe atoms was estimated to be 0.25 μ_B ($x = 1.0$) and 0.22 μ_B ($x = 1.3$). The zero quadrupole shift indicates a cubic symmetry in the local environment of Fe atoms as is expected for Fe atoms on the 4b site in the X_a structure. In the MFG/Cr sample with $x = 0.8$ composed of the tetragonal and cubic phases, a second magnetic component (blue line) with a larger $H_{\text{int}} \sim$ 16.5 T was observed in addition to the small H_{int} component (gold line) comparable to the cubic MFG/Cr samples. The Fe magnetic moment for this second component is estimated to be $M_{\text{Fe}} = 1.3$ μ_B. The quadrupole shift for this second component is also calculated to be $2\varepsilon \sim 0.2$ mm/s. Both its H_{int} and 2ε are of a similar magnitude to that reported for MFG with the DO₂₂ structure [53,54]. However, the broad hyperfine field distribution (ΔH_{int}) suggests the presence of considerable chemical disorder in the tetragonal phase.

The theoretical calculations for X_a-ordered Mn₂FeGa with $\lambda = 4.1\%$, which corresponds to the experimental value for the stoichiometric cubic MFG/Cr sample ($a = 5.83$ Å and $c = 6.07$ Å), successfully reproduced the Mössbauer results for the cubic MFG/Cr samples. The theoretically computed Fe magnetic moment of 0.21 μ_B closely matches the experimental values (0.25 μ_B and 0.22 μ_B) for the samples with $x = 1.0$ and $x = 1.3$. For the L2₁B-ordered state with disorder between the Mn 4a and Fe 4b sites, the moment was found to reduce to 0.11 μ_B. In contrast, for the D0₃-ordered state with disorder between the Mn 4c and Fe 4b sites, this type of disorder was found to lead to a significant increase in the Fe magnetic moment (1.99 μ_B). Importantly, the L2₁B-type disorder was shown to give rise to a relatively small change to the total density of states (DOS) and have a minor influence on the spin polarization around the Fermi level, whereas the D0₃-type disorder induces a drastic change to the total DOS and spin polarization (see the Supplemental Material [45]). Since in any of these cubic MFG/Cr samples ($x = 1.0$ and $x = 1.3$) there was no observation of the magnetic component with a large H_{int} (~ 25 T) as expected from the large Fe mag-
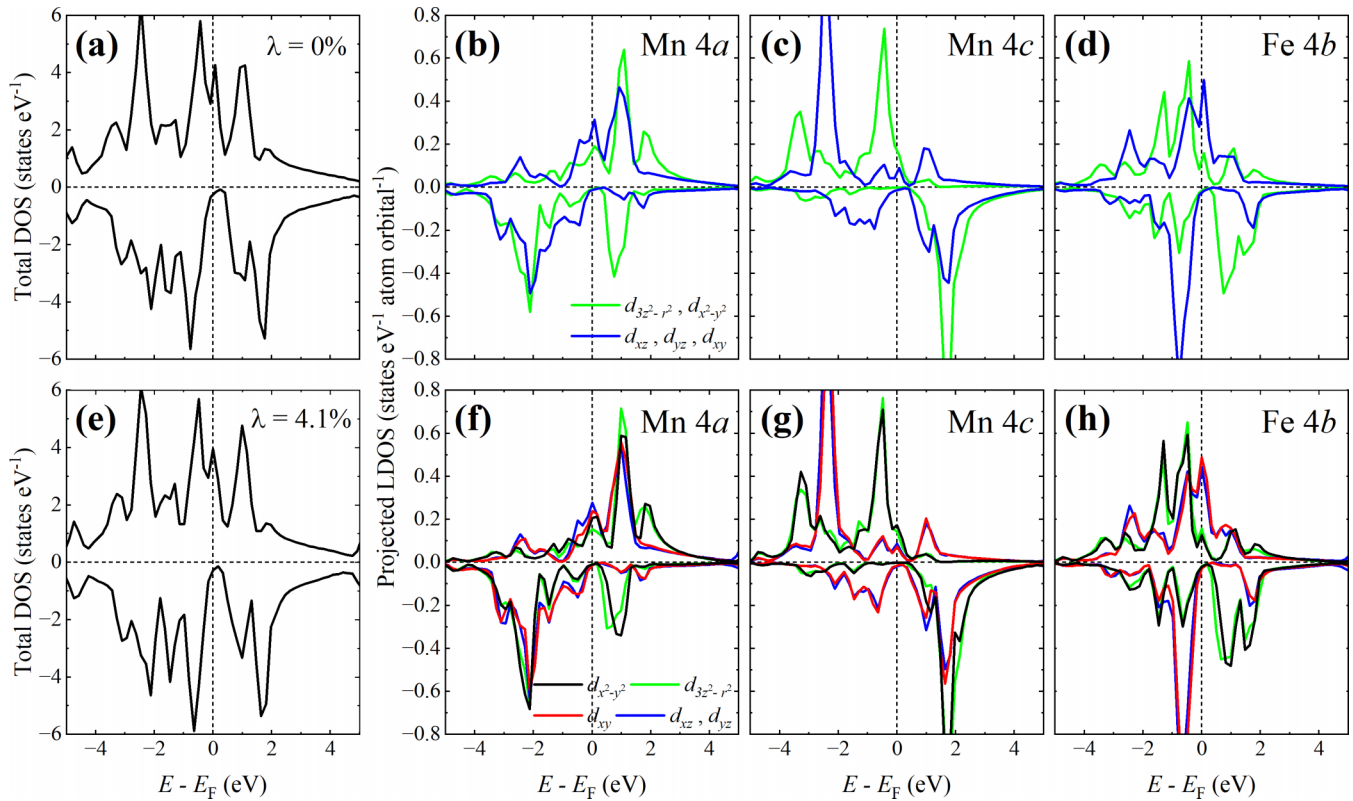
FIG. 5. (a) Total DOS for X_a-ordered Mn$_2$FeGa without tetragonal strain ($\lambda = 0\%$). (b)–(d) Projected LDOSs for this ordered state of the Mn $4a$, Mn $4c$, and Fe $4b$ atoms, respectively. (e) Total DOS for X_a-ordered Mn$_2$FeGa with $\lambda = 4.1\%$ and (f)–(h) LDOS for this case, respectively.

netic moment in the D0$_3$-ordered state, this result indicates the absence of the D0$_3$-type disorder which can significantly decrease the spin polarization of cubic MFG. Although it is difficult to discuss the presence of the L2$_1$B-type disorder due to its small hyperfine field expected from its small Fe magnetic moment, the reduction in M_s in the range of $x > 1$ is reasonably explained by an increase in antisite defects due to the substitution of Mn atoms in the Mn $4a$ sites with excess Fe atoms with a smaller magnetic moment in the X_a-ordered and/or L2$_1$B-ordered state in a similar manner to the calculations for stoichiometric Mn$_2$FeGa. Furthermore, the excellent agreement between the experimental Fe magnetic moment in the stoichiometric MFG/Cr sample and the theoretical value for the X_a-ordered state provides a direct proof of the formation of the X_a phase with a high degree of chemical ordering in the cubic Mn$_2$FeGa thin film.

D. Electronic band structure and origin of large PMA

The total DOS and projected local DOS (LDOS) of cubic Mn$_2$FeGa for the ideal X_a-ordered state without lattice distortion were calculated as shown in Figs. 5(a)–5(d). As seen in Fig. 5(a), X_a-ordered Mn$_2$FeGa is highly spin polarized with a spin polarization $\approx 92\%$ due to the half-metallic-like band structure with a pseudogap in the minority spin band. The half-metallic nature of MFG is attributed to hybridization between the Mn $4a$ and Fe $4b$ t_{2g} states which results in a prominent peak around the Fermi level (E_F) in the majority spin band while a gap opens up in the minority

spin band due to the Fe e_g and t_{2g} states being well separated [22]. Applying $\lambda = 4.1\%$ results in the DOS seen in Figs. 5(e)–5(h). Despite the lattice strain, the overall DOS remains mostly unchanged with only a minor reduction to the spin polarization from 92% to 87%. Small changes to the spin polarization under the strain can be explained as a result of changes in the distance between the Mn $4a$ and Fe $4b$ atoms which lead to a slight broadening of the states near the Fermi level in the minority spin band and reduction in states in the majority spin band; however, they do not raise the degeneracy of the Fe t_{2g} states which would wash away the peak in the majority spin band and fill the gap in the minority spin band, as reported for tetragonal MFG [22]. The above results demonstrate that the tetragonal strain preserves the half-metallic nature of cubic MFG and does not lead to significant changes to the spin polarization.

To see the effect of the tetragonal strain in cubic MFG on the strength of PMA observed, the uniaxial magnetocrystalline anisotropy K_u was calculated for the X_a-ordered state of Mn$_2$FeGa as a function of the strain λ by changing c while maintaining a constant a. As shown in Fig. 6, K_u was found to sharply increase with increasing λ, and a large K_u of 0.70 MJ m^{-3}, which is close to the experimentally observed value ($\geqslant 0.75$ MJ m^{-3}), was obtained for $\lambda = 4.1\%$. This indicates that the tetragonal strain in cubic MFG is essential for the generation of the large PMA.

Figure 7 shows results of the second-order perturbation analysis of the magnetocrystalline anisotropy energy, where E_{MCA}^i is the magnetocrystalline anisotropy energy at site i
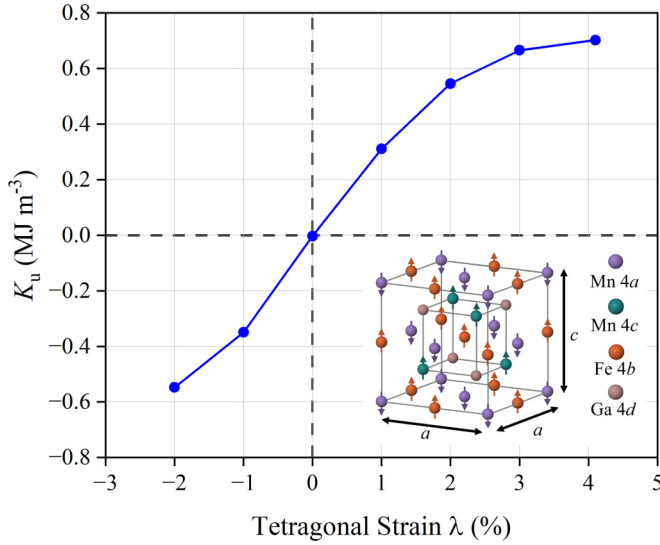
FIG. 6. The tetragonal strain λ dependence of K_u. The inset is the theoretical model of the X_a-ordered state of cubic Mn₂FeGa.

of X_a-ordered Mn₂FeGa, $\Delta E^i_{\uparrow\Rightarrow\uparrow}$ and $\Delta E^i_{\downarrow\Rightarrow\downarrow}$ are the spin-conserving terms in the majority and minority spin states, and $\Delta E^i_{\uparrow\Rightarrow\downarrow}$ and $\Delta E^i_{\downarrow\Rightarrow\uparrow}$ are the spin-flip terms from the majority to minority spin states and from the minority to majority spin states, respectively. Note here that $\Delta E^i_{\uparrow\Rightarrow\uparrow}$ and $\Delta E^i_{\uparrow\Rightarrow\downarrow}$ are given by the following equations:

$$\Delta E^i_{\uparrow\Rightarrow\uparrow} = \xi_i^2 \sum_{u_\uparrow, o_\uparrow} \frac{\left|\langle u_\uparrow | L_z^i | o_\uparrow \rangle\right|^2 - \left|\langle u_\uparrow | L_x^i | o_\uparrow \rangle\right|^2}{\epsilon_{u_\uparrow} - \epsilon_{o_\uparrow}}, \quad (7)$$

$$\Delta E^i_{\uparrow\Rightarrow\downarrow} = \xi_i^2 \sum_{u_\downarrow, o_\uparrow} \frac{\left|\langle u_\downarrow | L_x^i | o_\uparrow \rangle\right|^2 - \left|\langle u_\downarrow | L_z^i | o_\uparrow \rangle\right|^2}{\epsilon_{u_\downarrow} - \epsilon_{o_\uparrow}}, \quad (8)$$
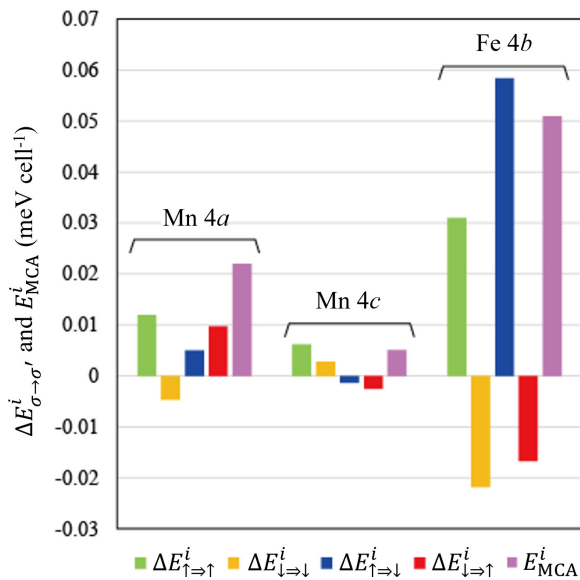

FIG. 7. The results of the second-order perturbation analysis of the magnetocrystalline anisotropy energy for cubic Mn₂FeGa with $\lambda = 4.1\%$.

where ξ_i is the spin-orbit coupling constant, L_α^i ($\alpha = x, z$) is the local angular momentum operator at site i, and $|o_\sigma\rangle$ ($|u_\sigma\rangle$) is the local occupied (unoccupied) state with spin σ and energy ϵ_{o_σ} (ϵ_{u_σ}). The majority and minority spin states are indicated by the up and down arrows, respectively. By comparing the values of ΔE^i between the Mn 4a, Mn 4c, and Fe 4b atoms, it was found that the $\Delta E^i_{\uparrow\Rightarrow\uparrow}$ and $\Delta E^i_{\uparrow\Rightarrow\downarrow}$ for the Fe 4b atoms have large positive values and are contributing dominantly to E^i_{MCA}. The origin of the large $E^i_{\uparrow\Rightarrow\uparrow}$ and $\Delta E^i_{\uparrow\Rightarrow\downarrow}$ of Fe can be understood from the projected local density of states (LDOS) shown in Fig. 5(h). In the majority spin channel in Fig. 5(h), the $d_{x^2-y^2}$ orbital has a large LDOS in the occupied state close to E_F, while the d_{xy} states has a large LDOS across E_F. This characteristic electronic structure of Fe around E_F results in a large value of $\langle d_{xy}, \uparrow | L_z | d_{x^2-y^2}, \uparrow \rangle$ in Eq. (7), by which $E^i_{\uparrow\Rightarrow\uparrow}$ has a large positive value. In a similar manner, the large density of the occupied $|d_{xz}(d_{yz}), \uparrow \rangle$ states and unoccupied $|d_{3z^2-r^2}, \downarrow \rangle$ states of Fe close to E_F give a large value of $\langle d_{3z^2-r^2}, \downarrow | L_x | d_{xz}(d_{yz}), \uparrow \rangle$ in Eq. (8), thus providing a large positive value $\Delta E^i_{\uparrow\Rightarrow\downarrow}$. It is worth noting that no such electronic features of the Y atoms around E_F have been observed in other cubic Mn₂YZ-type Heusler compounds (Y $\neq$ Fe) [20]. This explains why the buffer layer induced PMA in cubic MFG is remarkably stronger than that in other ferrimagnetic cubic Heusler compounds [18,29].

V. SUMMARY

In summary high-quality cubic-type full-Heusler Mn₂Fe$_x$Ga ($x = 1.0$–1.3) thin films were successfully prepared by using a Cr buffer layer. The stoichiometric cubic MFG thin film ($x = 1.0$) showed a small saturation magnetization of 1.2 μ_B/f.u. in good agreement with the Slater-Pauling rule. Most strikingly, the stoichiometric cubic MFG thin film was found to exhibit a large PMA at least as large as $K_u = 0.75$ MJ m^{-3} in the presence of a tetragonal strain. Using synchrotron Mössbauer spectroscopy, an atomic magnetic moment of Fe, $M_{\mathrm{Fe}} = 0.25$ μ_B, was observed which is close to the theoretically predicted value for the X_a-ordered state indicating the growth of cubic Mn₂FeGa with a high degree of chemical ordering. First-principles calculations demonstrated that the origin of the large PMA is due to the specific features of Fe d orbitals located around the Fermi level, which give rise to a large uniaxial magnetocrystalline anisotropy under the strain; and, furthermore, that the high spin polarization of cubic MFG due to its half-metallic nature can be preserved even under the tetragonal strain. The large PMA, small saturation magnetization, as well as the possibility of it being highly spin polarized as revealed in this study make cubic MFG a suitable candidate for the development of next-generation spintronic devices such as magnetic random-access memory.

[1] T. Graf, C. Felser, and S. S. P. Parkin, Heusler Compounds: Applications in Spintronics, in *Handbook of Spintronics*, edited by Y. Xu, D. D. Awschalom, and J. Nitta (Springer Netherlands, Dordrecht, 2016), pp. 335–364.

[2] K. Elphick, W. Frost, M. Samiepour, T. Kubota, K. Takanashi, H. Sukegawa, S. Mitani, and A. Hirohata, Sci. Technol. Adv. Mater. **22**, 235 (2021).

[3] Y. Sakuraba, M. Hattori, M. Oogane, Y. Ando, H. Kato, A. Sakuma, T. Miyazaki, and H. Kubota, Appl. Phys. Lett. **88**, 192508 (2006).

[4] H.-x. Liu, Y. Honda, T. Taira, K.-I. Matsuda, M. Arita, T. Uemura, and M. Yamamoto, Appl. Phys. Lett. **101**, 132418 (2012).

[5] Y. K. Takahashi, S. Kasai, S. Hirayama, S. Mitani, and K. Hono, Appl. Phys. Lett. **100**, 052405 (2012).

[6] S. Li, Y. K. Takahashi, T. Furubayashi, and K. Hono, Appl. Phys. Lett. **103**, 042405 (2013).

[7] M. Yamada, F. Kuroda, M. Tsukahara, S. Yamada, and T. Fukushima, NPG Asia Mater. **12**, 47 (2020).

[8] R. Shan, H. Sukegawa, W. H. Wang, M. Kodzuka, T. Furubayashi, T. Ohkubo, S. Mitani, K. Inomata, and K. Hono, Phys. Rev. Lett. **102**, 246601 (2009).

[9] M. Jourdan, J. Minár, J. Braun, A. Kronenberg, S. Chadov, B. Balke, A. Gloskovskii, M. Kolbe, H. J. Elmers, G. Schönhense, H. Ebert, C. Felser, and M. Kläui, Nat. Commun. **5**, 3974 (2014).

[10] C. Guillemard, S. Petit-Watelot, L. Pasquier, D. Pierre, J. Ghanbaja, J.-C. Rojas-Sánchez, A. Bataille, J. Rault, P. Le Fèvre, F. Bertran, and S. Andrieu, Phys. Rev. Appl. **11**, 064009 (2019).

[11] J. M. Shaw, E. K. Delczeg-Czirjak, E. R. J. Edwards, Y. Kvashnin, D. Thonig, M. A. W. Schoen, M. Pufall, M. L. Schneider, T. J. Silva, O. Karis, K. P. Rice, O. Eriksson, and H. T. Nembach, Phys. Rev. B **97**, 094420 (2018).

[12] A. Kumar, F. Pan, S. Husain, S. Akansel, R. Brucas, L. Bergqvist, S. Chaudhary, and P. Svedlindh, Phys. Rev. B **96**, 224425 (2017).

[13] C. Guillemard, W. Zhang, G. Malinowski, C. de Melo, J. Gorchon, S. Petit-Watelot, J. Ghanbaja, S. Mangin, P. L. Fèvre, F. Bertran, and S. Andrieu, Adv. Mater. **32**, 1908357 (2020).

[14] I. Belopolski, K. Manna, D. S. Sanchez, G. Chang, B. Ernst, J. Yin, S. S. Zhang, T. Cochran, N. Shumiya, H. Zheng, B. Singh, G. Bian, D. Multer, M. Litskevich, X. Zhou, S.-M. Huang, B. Wang, T.-R. Chang, S.-Y. Xu, A. Bansil *et al.*, Science **365**, 1278 (2019).

[15] K. Tang, Z. Wen, Y.-C. Lau, H. Sukegawa, T. Seki, and S. Mitani, Appl. Phys. Lett. **118**, 062402 (2021).

[16] S. Ikeda, K. Miura, H. Yamamoto, K. Mizunuma, H. D. Gan, M. Endo, S. Kanai, J. Hayakawa, F. Matsukura, and H. Ohno, Nat. Mater. **9**, 721 (2010).

[17] H. Kurt, K. Rode, P. Stamenov, M. Venkatesan, Y.-C. Lau, E. Fonda, and J. M. D. Coey, Phys. Rev. Lett. **112**, 027201 (2014).

[18] T. Kubota, D. Takano, Y. Kota, S. Mohanty, K. Ito, M. Matsuki, M. Hayashida, M. Sun, Y. Takeda, Y. Saitoh, S. Bedanta, A. Kimura, and K. Takanashi, Phys. Rev. Mater. **6**, 044405 (2022).

[19] C. Banerjee, N. Teichert, K. E. Siewierska, Z. Gercsi, G. Y. P. Atcheson, P. Stamenov, K. Rode, J. M. D. Coey, and J. Besbas, Nat. Commun. **11**, 4444 (2020).

[20] L. Wollmann, S. Chadov, J. Kübler, and C. Felser, Phys. Rev. B **90**, 214420 (2014).

[21] H. Z. Luo, H. W. Zhang, Z. Y. Zhu, L. Ma, S. F. Xu, G. H. Wu, X. X. Zhu, C. B. Jiang, and H. B. Xu, J. Appl. Phys. **103**, 083908 (2008).

[22] A. Kundu and S. Ghosh, Intermetallics **93**, 209 (2018).

[23] A. Kalache, S. Selle, W. Schnelle, G. H. Fecher, T. Höche, C. Felser, and A. Markou, Phys. Rev. Mater. **2**, 084407 (2018).

[24] D. Betto, Y.-C. Lau, K. Borisov, K. Kummer, N. B. Brookes, P. Stamenov, J. M. D. Coey, and K. Rode, Phys. Rev. B **96**, 024408 (2017).

[25] F. Wu, S. Mizukami, D. Watanabe, H. Naganuma, M. Oogane, Y. Ando, and T. Miyazaki, Appl. Phys. Lett. **94**, 122503 (2009).

[26] L. Zhu, S. Nie, K. Meng, D. Pan, J. Zhao, and H. Zheng, Adv. Mater. **24**, 4547 (2012).

[27] S. Mao, J. Lu, X. Zhao, X. Wang, D. Wei, J. Liu, J. Xia, and J. Zhao, Sci. Rep. **7**, 43064 (2017).

[28] H. Kurt, N. Baadji, K. Rode, M. Venkatesan, P. Stamenov, S. Sanvito, and J. M. D. Coey, Appl. Phys. Lett. **101**, 132410 (2012).

[29] K. E. Siewierska, G. Atcheson, K. Borisov, M. Venkatesan, K. Rode, and J. M. D. Coey, IEEE Trans. Magn. **53**, 2600505 (2017).

[30] T. Mitsui, N. Hirao, Y. Ohishi, R. Masuda, Y. Nakamura, H. Enoki, K. Sakaki, and M. Seto, J. Synchrotron Radiat. **16**, 723 (2009).

[31] T. Mitsui, K. Mibu, M. Tanaka, S. Kitao, Y. Kobayashi, R. Masuda, and M. Seto, J. Phys. Soc. Jpn. **89**, 054707 (2020).

[32] T. Mitsui, M. Seto, R. Masuda, Y. Kobayashi, and S. Kitao, Jpn. J. Appl. Phys. **47**, 7136 (2008).

[33] G. Kresse and J. Furthmüller, Phys. Rev. B **54**, 11169 (1996).

[34] J. P. Perdew, K. Burke, and M. Ernzerhof, Phys. Rev. Lett. **77**, 3865 (1996).

[35] P. E. Blöchl, Phys. Rev. B **50**, 17953 (1994).

[36] G. Kresse and D. Joubert, Phys. Rev. B **59**, 1758 (1999).

[37] G. H. O. Daalderop, P. J. Kelly, and M. F. H. Schuurmans, Phys. Rev. B **41**, 11919 (1990).

[38] M. Weinert, R. E. Watson, and J. W. Davenport, Phys. Rev. B **32**, 2115 (1985).

[39] Y. Miura, S. Ozaki, Y. Kuwahara, M. Tsujikawa, K. Abe, and M. Shirai, J. Phys.: Condens. Matter **25**, 106005 (2013).

[40] T. Hahn, *International Tables for Crystallography* (Kluwer Academic, Dordrecht, 2002), Chap. 1.

[41] J. Korringa, Physica **13**, 392 (1947).

[42] W. Kohn and N. Rostoker, Phys. Rev. **94**, 1111 (1954).

[43] AkaiKKR home web page, accessed 2012-11-25 (2023), http://kkr.issp.u-tokyo.ac.jp.

[44] J. W. Koo, S. Mitani, T. T. Sasaki, H. Sukegawa, Z. C. Wen, T. Ohkubo, T. Niizeki, K. Inomata, and K. Hono, Appl. Phys. Lett. **103**, 192401 (2013).

[45] See Supplemental Material at http://link.aps.org/supplemental/10.1103/PhysRevMaterials.7.064404 for an AFM image of the MFG surface, magnetization curves for the different MFG/Cr samples, alternative fitting for the $x = 1.0$ Mössbauer spectrum, computational methods and results for the different ordered and disordered states of cubic MFG, and selected area electron diffraction patterns taken from the stoichiometric MFG/Cr sample.

[46] A. Niesen, C. Sterwerf, M. Glas, J.-M. Schmalhorst, and G. Reiss, IEEE Trans. Magn. **52**, 1 (2016).

[47] S. Kurdi, Y. Sakuraba, K. Masuda, H. Tajiri, B. Nair, G. F. Nataf, M. E. Vickers, G. Reiss, M. Meinert, S. S. Dhesi, M. Ghidini, and Z. H. Barber, J. Phys. D: Appl. Phys. **55**, 185305 (2022).

[48] I. Galanakis, P. H. Dederichs, and N. Papanikolaou, Phys. Rev. B **66**, 174429 (2002).

[49] S. Skaftouros, K. Özdoğan, E. Şaşıoğlu, and I. Galanakis, Phys. Rev. B **87**, 024420 (2013).

[50] T. Schrefl, J. Fidler, and H. Kronmüller, Phys. Rev. B **49**, 6100 (1994).

[51] D. G. Rancourt and J. Y. Ping, Nucl. Instrum. Methods Phys. Res. Sect. B **58**, 85 (1991).

[52] T. Gasi, V. Ksenofontov, J. Kiss, S. Chadov, A. K. Nayak, M. Nicklas, J. Winterlik, M. Schwall, P. Klaer, P. Adler, and C. Felser, Phys. Rev. B **87**, 064411 (2013).

[53] A. Koeba, T. Shima, and M. Doi, Jpn. J. Appl. Phys. **55**, 07MC04 (2016).

[54] T. Gasi, A. K. Nayak, J. Winterlik, V. Ksenofontov, P. Adler, M. Nicklas, and C. Felser, Appl. Phys. Lett. **102**, 202402 (2013).